



Cite this: *Green Chem.*, 2025, **27**, 8226

# Fluorine-free polysiloxane-based single-ion-conducting polymer electrolyte for lithium–metal batteries†

Leo Gräber, <sup>a,b</sup> Vittorio Marangon, <sup>\*a,b</sup> Manish Kumar, <sup>a,b</sup> Marcel Weil <sup>a,b</sup> and Dominic Bresser <sup>\*a,b,c</sup>

Herein, the synthesis and comprehensive characterization of a new, completely fluorine-free single-ion-conducting polymer electrolyte (SIPE) for lithium–metal batteries are reported. For this new SIPE, lithium (4-styrenesulfonyl)(dicyanomethide) has been grafted onto a polysiloxane backbone. Self-standing membranes additionally containing non-toxic polyacrylonitrile and propylene carbonate exhibit suitable mechanical properties, a high ionic conductivity of more than  $10^{-4}$  S cm<sup>-1</sup>, and good anodic stability up to more than 4.1 V vs. Li<sup>+</sup>/Li at 40 °C. Symmetric Li||Li cells show an excellent cycle life with more than 1000 h of lithium stripping and plating, thanks to the formation of a stable and low-resistive interphase. As a result, completely fluorine-free Li||LiFePO<sub>4</sub> cells provide stable cycling for more than 500 cycles, rendering this new electrolyte system very promising for the realization of more sustainable and safer lithium batteries.

Received 15th January 2025,  
Accepted 16th May 2025

DOI: 10.1039/d5gc00252d

[rsc.li/greenchem](https://rsc.li/greenchem)

## Green foundation

1. This work proposes a new single-ion-conducting polymer electrolyte relying on a sustainable, completely fluorine-free composition to achieve safer, high-performance lithium batteries.
2. The polymer electrolyte is prepared *via* a simple synthesis route, with yields well above 75%. The inclusion of non-toxic polyacrylonitrile allows for the preparation of self-standing electrolyte membranes. Li||LiFePO<sub>4</sub> cells employing this new electrolyte and fluorine-free cathodes provide stable cycling for more than 500 cycles and good performance even when increasing the active material loading to almost 10 mg cm<sup>-2</sup>.
3. Future research will focus on further increasing the active material mass loading and substituting lithium metal with alternative anode materials to obtain intrinsically safe, truly sustainable, low-cost, high-performance lithium-ion polymer batteries.

## Introduction

Lithium-ion batteries (LIBs) are often acknowledged as a key technology for driving a successful clean-energy transition due to their highly versatile applications, especially in portable electronic devices, electric vehicles and grid-storage plants.<sup>1–3</sup> However, after extensive research, the specific capacity of LIBs

relying on graphite- or silicon-based anodes is about to reach their theoretical limits.<sup>4,5</sup> The replacement of the anode with metallic lithium is expected to significantly increase the energy density due to its superior capacity and negative potential (3861 mA h g<sup>-1</sup>, −3.040 V vs. SHE).<sup>6–8</sup> However, lithium–metal batteries (LMBs) face serious challenges, particularly in regard to the formation of a stable solid electrolyte interphase (SEI) on the lithium surface and safety.<sup>8–10</sup> The latter is undermined by the risk of dendrite formation, which can lead to short circuits and thermal runaway of the cell.<sup>11,12</sup> Thus, the stabilization of the Li|electrolyte interface is mandatory for widespread commercialization of LMBs.<sup>13,14</sup> Several strategies have been implemented to address this issue, including host structures for the Li metal electrode,<sup>15,16</sup> the design of artificial SEIs,<sup>17,18</sup> and the utilization of solid electrolytes, *e.g.* sulfides,<sup>19–21</sup> ceramics<sup>22,23</sup> or polymers.<sup>7,24–28</sup> The latter represents a promising approach as polymers provide concomi-

<sup>a</sup>Helmholtz Institute Ulm (HIU), Helmholtzstrasse 11, 89081 Ulm, Germany.

E-mail: [vittorio.marangon@kit.edu](mailto:vittorio.marangon@kit.edu), [dominic.bresser@kit.edu](mailto:dominic.bresser@kit.edu)

<sup>b</sup>Karlsruhe Institute of Technology (KIT), P.O. Box 3640, 76021 Karlsruhe, Germany

<sup>c</sup>Ulm University (UUlm), 89069 Ulm, Germany

†Electronic supplementary information (ESI) available: Photographic images and additional experimental data including <sup>13</sup>C NMR spectra, TGA profiles, Nyquist plots recorded by EIS, XRD patterns, voltage profiles related to Li stripping/plating tests and chronoamperometric curves. Appendix 1 (F-free SIPE) and Appendix 2 (PSiOM). See DOI: <https://doi.org/10.1039/d5gc00252d>



tantly high safety, potentially low-cost synthesis from abundant starting materials, good processability, and favorable mechanical properties.<sup>29,30</sup> Nevertheless, a key issue is the ionic conductivity, which usually ranges between  $10^{-5}$  and  $10^{-7}$  S cm<sup>-1</sup>, *i.e.*, well below the conductivity of liquid electrolytes ( $\sim 10^{-3}$  S cm<sup>-1</sup>).<sup>24–26</sup> Additionally, conventional salt-in-polymer electrolytes suffer from significantly higher anion mobility compared to the lithium cations, resulting in a very low lithium transference number ( $t_{\text{Li}^+} < 0.5$ ).<sup>31</sup> This limits the cell performance owing to the potential buildup of reversed polarization gradients, which may cause uneven deposition of lithium, promoting dendrite formation.<sup>32–34</sup> A possible solution lies in the use of single-ion conducting polymer electrolytes (SIPEs), in which the negative charge carrier is a weakly coordinating anion, covalently bonded to or incorporated into the polymer chain.<sup>24,35</sup> In particular, highly fluorinated sulfonates and sulfonylimides derived from the widely used lithium bis(trifluoromethanesulfonyl)imide (as the conducting salt) are usually preferred due to the significant charge delocalization triggered by strongly electron-withdrawing sulfonyl and trifluoromethane units,<sup>35–38</sup> while fluorine allows for the formation of a LiF-rich SEI, which reportedly improves the cell performance.<sup>39–41</sup> Moreover, fluorinated compounds usually offer improved thermal and electrochemical stability with respect to F-free homologues.<sup>40,41</sup> However, the toxicity and persistency of fluorinated materials raise serious concerns about their production costs and recycling, leading to major obstacles to the sustainability of related devices.<sup>42,43</sup> Thus, many efforts have recently focused on the development of novel F-free anions designed to retain the desirable properties of traditional fluorinated conducting salts for LIBs and LMBs, relying, for example, on borates,<sup>43,44</sup> phosphates,<sup>45</sup> or cyanides.<sup>46,47</sup> Despite the remarkable progress achieved in this field, to the best of our knowledge, only a handful of reports have proposed the development of fluorine-free SIPEs,<sup>47–49</sup> where the new electrolytes are usually applied in batteries relying on modest active material loadings at the cathode or on the use of harmful solvents for electrode processing.

Following this objective, we report herein the development of a novel fluorine-free SIPE employing the weakly coordinating lithium (4-styrenesulfonyl)(dicyanomethide) (LiSDM),<sup>47</sup> which is grafted *via* a thiol-ene click reaction to a thiol-functionalized polysiloxane backbone, poly[(mercaptopropyl)methylsiloxane] (PMMS), following a previous study in which we used lithium (3-methacryloyloxypropylsulfonyl)(trifluoromethylsulfonyl)imide as ionic side chain.<sup>50</sup> To yield self-standing, flexible, but still fluorine-free polymer electrolyte membranes, the resulting ionomer is blended with polyacrylonitrile (PAN) instead of the commonly used polyvinylidene fluoride (PVdF).<sup>51</sup> Swollen with 50 wt% propylene carbonate (PC), these SIPE membranes provide high ionic conductivity, long-term stable lithium stripping and plating for more than 1000 h, and good performance in Li||LiFePO<sub>4</sub> (LFP) cells, which are realized with a completely F-free configuration by substituting the commonly employed PVdF binder in the cathode with sodium carboxymethyl cellulose (CMC), allowing for the aqueous proces-

sing of the electrode. In addition, the possible scale-up of this novel configuration is explored by achieving LFP mass loadings exceeding 9 mg cm<sup>-2</sup>, benefitting from the incorporation of the F-free SIPE into the electrode to enhance the electrode|electrolyte interfacial contact and ionic conductivity within the cathode. Finally, a toxicity assessment of the F-free SIPE membrane is provided, comparing the herein developed F-free SIPE with an earlier reported F-containing SIPE. This comparison highlights the great progress towards the realization of less toxic electrolytes and provides a benchmark for future developments. Moreover, the work presented herein highlights the need to carefully evaluate any potential improvement concerning sustainability, going well beyond a “simple” judgement based on the absence of certain elements – even if highly desirable.

## Results and discussion

The synthesis of LiSDM and SIPE is schematically depicted in Fig. 1a. The LiSDM ionic side chain is synthesized by nucleophilic substitution of malononitrile on freshly prepared (4-styrene)sulfonyl chloride in the presence of a base. The acidic proton of the methide side group reacts further with aqueous LiOH as a strong base to form lithiated LiSDM. Both the <sup>1</sup>H and <sup>13</sup>C nuclear magnetic resonance (NMR) spectra (Fig. 1b and Fig. S1,† respectively) confirm the successful synthesis of LiSDM in agreement with previous literature.<sup>47</sup> Additionally, the Fourier transform infrared (FTIR) spectrum in Fig. 1c displays the characteristic band for C=C at 920 cm<sup>-1</sup>,<sup>52</sup> the symmetric and anti-symmetric O=S=O stretching at 1140 and 1300 cm<sup>-1</sup>, respectively,<sup>50,53</sup> and the C≡N stretching at 2190 cm<sup>-1</sup>, while the band at 2225 cm<sup>-1</sup> is induced by the interaction of Li<sup>+</sup> with the cyano group, leading to the favored formation of a C=C=N<sup>-</sup> iminium-type mesomeric structure.<sup>54,55</sup> The successful synthesis of the final SIPE, prepared by a thiol-ene click reaction between LiSDM and PMMS using azobisisobutyronitrile (AIBN) as a radical starter (Fig. 1a), is revealed by <sup>1</sup>H NMR and FTIR spectroscopy (Fig. 1b and c, respectively). In particular, the FTIR data show the preservation of the aforementioned bands for O=S=O and C≡N, while two additional peaks arise at 779 and 1073 cm<sup>-1</sup>, ascribed to Si–O–Si bonds.<sup>50,52</sup> The successful transition from LiSDM to the eventual SIPE is further corroborated by the aliphatic C–H bonds identified at 2920 cm<sup>-1</sup>.<sup>50,52</sup> The molecular weight of the final SIPE is determined *via* gel permeation chromatography (GPC), revealing a molecular mass of about 10–14 kg mol<sup>-1</sup> (*M<sub>n</sub>* and *M<sub>w</sub>* are provided in Table S1†).

Polymer electrolyte membranes were obtained by blending the SIPE with various contents of PAN (15, 25, 35, 45 and 55 wt%) to ensure adequate mechanical stability. The final membranes were denoted as B15, B25, B35, B45, and B55 (see the corresponding composition and a photograph in Table S2 and Fig. S2,† respectively). The decomposition temperatures of the B15–B55 membranes were determined *via* thermogravimetric analysis (TGA, Fig. S3a†) and are compared with



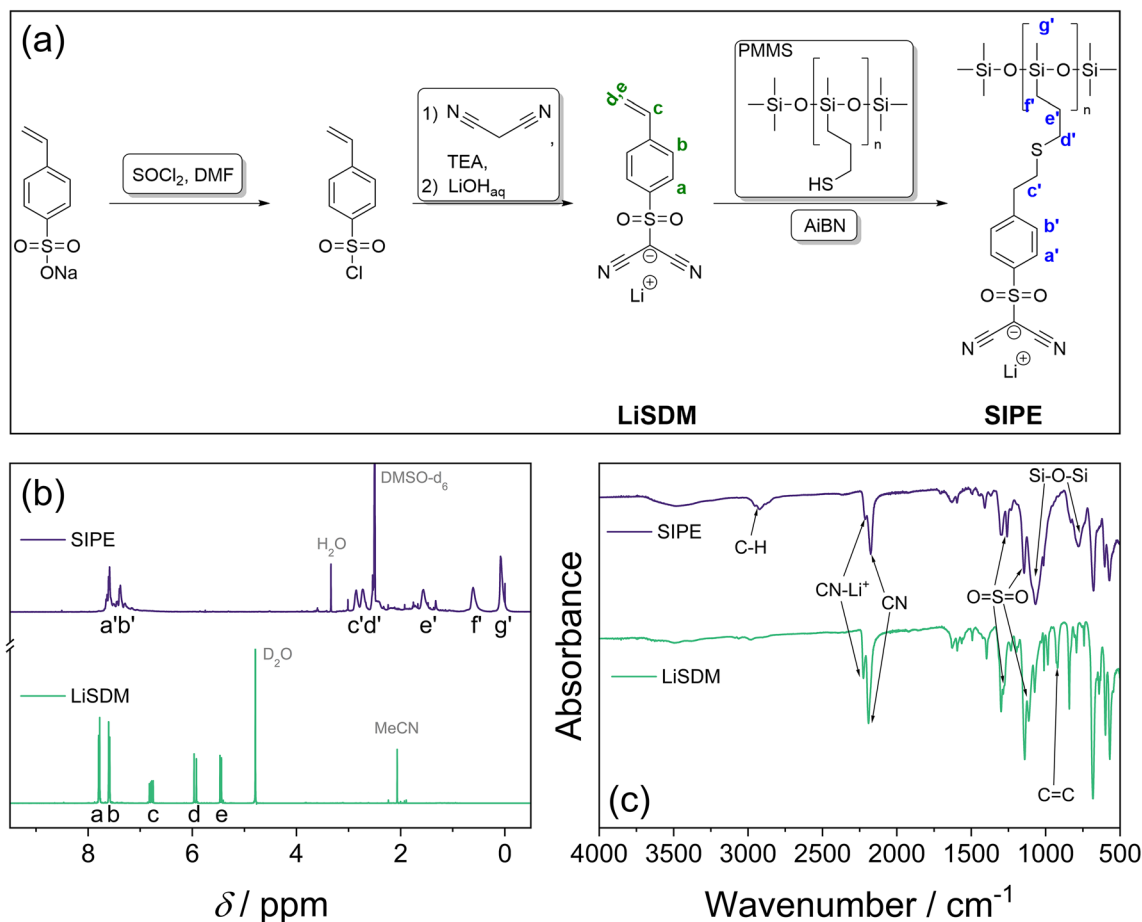


**Fig. 1** (a) Schematic representation of the synthesis pathway for the fluorine-free SIPE via LiSDM; (b)  $^1\text{H}$  NMR and (c) FTIR spectra of LiSDM (green) and SIPE (violet).

those of the neat SIPE and bare PAN in Fig. 2a, where the decomposition temperature is defined as the value at which a mass loss of 3 wt% occurs. The comparison reveals a significant dependence between the decomposition temperature and the PAN content, as expected from the large difference between the values recorded for the SIPE and bare PAN, *i.e.*, 120 and 285  $^{\circ}\text{C}$ , respectively. In particular, the decomposition temperatures show a quasi-logarithmic increase from B15 to B55 with the respective values of 127, 167, 193, 216, and 223  $^{\circ}\text{C}$ . This trend may be associated with modifications in the microstructure and morphology of the polymer blends linked to the increase of PAN content, which gradually drives the thermal behavior from a response similar to the SIPE (B15) to an intermediate one between the SIPE and PAN (B55).<sup>56,57</sup> Prior to the electrochemical measurements, the membranes were swollen with PC (50 wt% with respect to the membrane as determined *via* eqn (S1)† and TGA in Fig. S3b†), serving as a “molecular transporter” owing to its high dielectric constant to improve the ionic conductivity. Fig. 2b evaluates the anodic stability of the membranes determined *via* linear sweep voltammetry (LSV), showing values between 4.1 and 4.3 V *vs.*  $\text{Li}^+/\text{Li}$  (the limiting potential values are determined corresponding to an evolving current of  $2.5 \mu\text{A cm}^{-2}$ ), with no apparent influence of the

PAN content, though a higher PAN content appears generally favorable. In fact, the anodic stability is expected to be determined by the oxidizable thioether function in the SIPE,<sup>50,58</sup> while the minor signal observed for all the membranes slightly above 4.0 V *vs.*  $\text{Li}^+/\text{Li}$  may be ascribed to the presence of PC.<sup>50</sup> Although the addition of fluorinated species such as PVDF may significantly increase the anodic stability,<sup>25,59,60</sup> the F-free configuration proposed herein represents a more sustainable solution and still allows for application in LMBs employing cathodes operating at moderate voltage like LFP.<sup>40</sup> The ionic conductivity ( $\sigma$ ) was determined through electrochemical impedance spectroscopy (EIS) and the results are presented in the form of an Arrhenius plot in Fig. 2c (see the corresponding Nyquist plots in Fig. S4†). The comparison reveals the lowest  $\sigma$  for B15 between  $5.4 \times 10^{-6}$  and  $3.8 \times 10^{-4} \text{ S cm}^{-1}$  in the 10–90  $^{\circ}\text{C}$  range, followed by B55 and B45, while B25 exhibits values slightly lower than those associated with B35, which delivers the best  $\sigma$  between  $1.0 \times 10^{-4}$  and  $9.2 \times 10^{-4} \text{ S cm}^{-1}$ . This behavior may be due to an optimal microstructure of the B35 blend, while maintaining a suitable concentration of  $\text{Li}^+$  cations. At 40  $^{\circ}\text{C}$ , B35 exhibits an ionic conductivity of  $2.9 \times 10^{-4} \text{ S cm}^{-1}$ , which appears suitable for potential commercial applications of such SIPE-based electro-



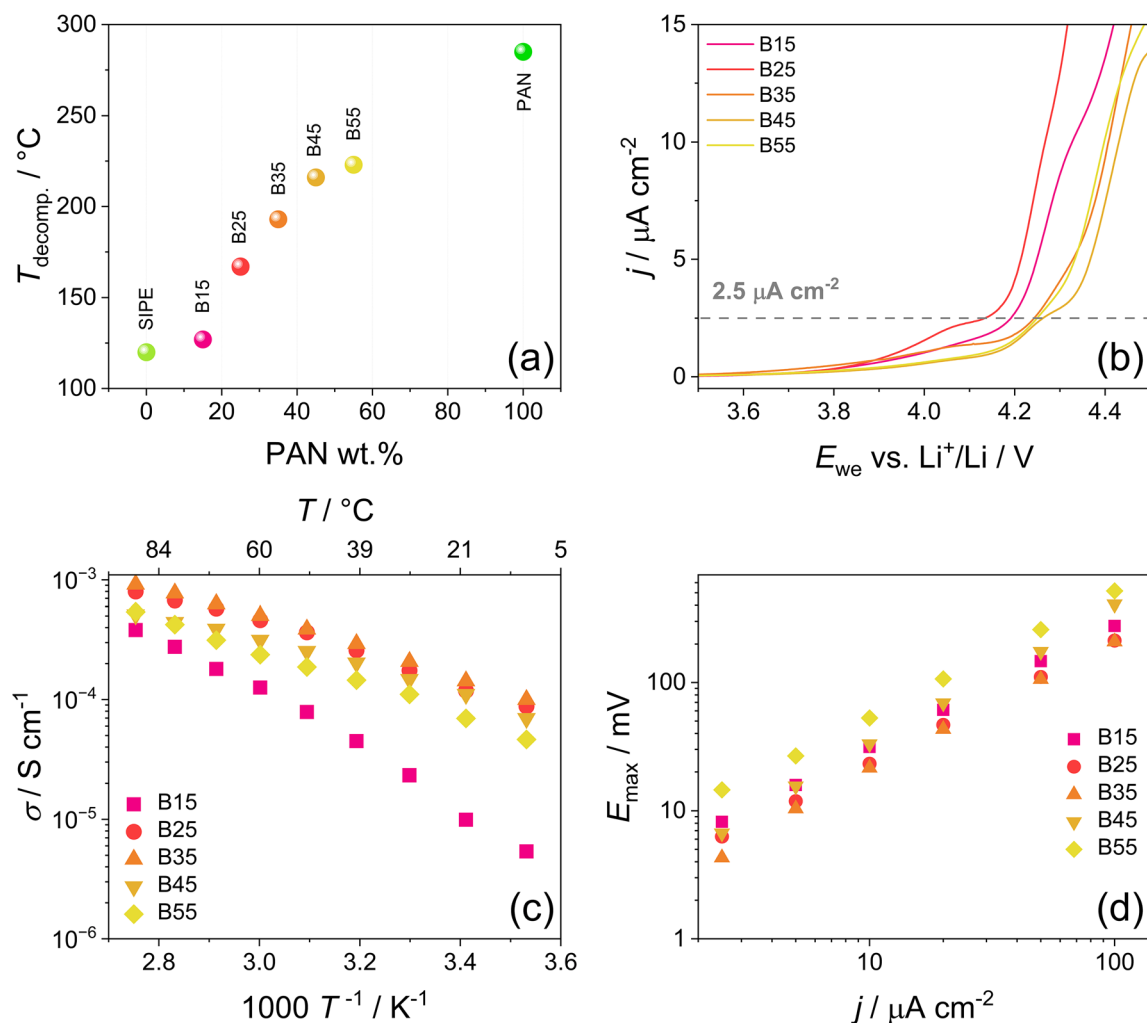


**Fig. 2** Thermal and basic electrochemical characterization of the B15–B55 membranes: (a) decomposition temperature determined *via* TGA (see Fig. S3a† for the thermograms) and comparison with those of the neat SIPE and bare PAN; (b) anodic stability evaluated through LSV between open circuit voltage (OCV) and 6.0 V vs.  $\text{Li}^+/\text{Li}$  using a sweep rate of  $0.1 \text{ mV s}^{-1}$  at  $40^\circ\text{C}$ ; (c) Arrhenius plots of ionic conductivity obtained *via* EIS (see the Nyquist plots in Fig. S4†) between 10 and  $90^\circ\text{C}$  in the 1.0 MHz–1 Hz frequency range (voltage amplitude: 10 mV); (d) overpotential values related to the Li stripping/plating tests carried out at various current densities at  $40^\circ\text{C}$  (see the corresponding voltage profiles in Fig. S5†).

lytes.<sup>32</sup> The compatibility of the membranes with metallic lithium was evaluated through Li stripping/plating tests in symmetric  $\text{Li}||\text{Li}$  cells by galvanostatic cycling at increasing current densities (see Fig. S5†). The overall trend is displayed in Fig. 2d, revealing the expected increase in overpotentials for all the electrolytes with increasing current density, with the lowest overpotential values for B35, *i.e.*, from  $\sim 4.3$  to  $\sim 208 \text{ mV}$  in the  $2.5$ – $100 \mu\text{A cm}^{-2}$  current density range. Considering the above results, especially in terms of  $\sigma$  and overpotential, B35 was selected as the most promising candidate for the forthcoming experiments.

The structure and morphology of the dry B35 membrane were investigated *via* X-ray diffraction (XRD) and scanning electron microscopy (SEM) coupled with energy dispersive X-ray spectroscopy (EDX). The XRD patterns recorded for bare PAN, the SIPE powder, and the B35 membrane, as presented in Fig. S6,† reveal for the latter the combination of the amorphous

SIPE, as indicated by the broad reflection centered around  $19^\circ$ ,<sup>61</sup> and the partially crystalline nature of PAN, as indicated by the retention of the prominent reflection at  $17^\circ$ , which has been attributed to the planar spacing of the polymer chains,<sup>62,63</sup> while its intensity is substantially reduced. The homogeneous blending of the SIPE and PAN is evidenced by the SEM-EDX analyses presented in Fig. 3a–f. The SEM micrographs (Fig. 3a and b) display a homogeneous and smooth surface of the B35 membrane, without any indication of agglomerates, along with the presence of sub-micrometric pores that may favor the uptake of PC molecules. The EDX mapping of silicon, nitrogen, sulfur, and carbon confirms a uniform distribution of these elements, thus corroborating a successful and homogeneous blending of the two polymers (Fig. 3c–f).

The  $\text{Li}^+$  transference number ( $t^+$ ) of the B35 membrane was determined using the Bruce–Vincent–Evans method (Fig. S7†).<sup>64,65</sup> The data collected from the chronoampero-



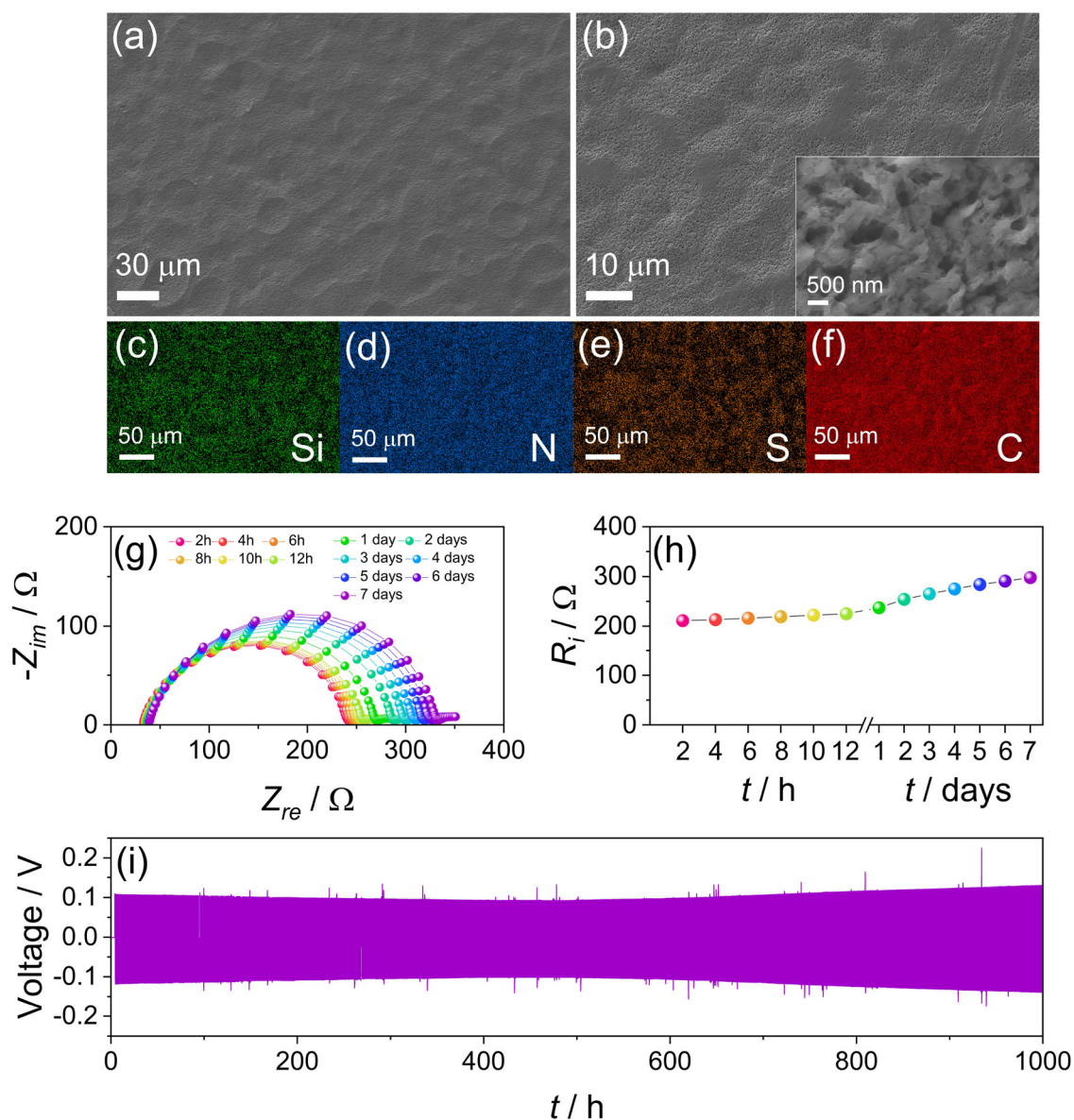


**Fig. 3** Evaluation of the morphology of B35 and its behavior in symmetric Li||Li cells: (a and b) SEM micrographs at different magnifications and (c–f) the corresponding EDX mapping for (c) Si, (d) N, (e) S, and (f) C; (g) Nyquist plots recorded by EIS for a Li||Li cell in the 200 kHz–50 mHz frequency range (voltage amplitude: 10 mV) upon calendar aging and (h) the trend of the corresponding electrode|electrolyte interphase resistance ( $R_i$ ) determined through NLLS fitting (see Table S4† for the actual values); (i) voltage profiles related to the long-term Li stripping/plating test performed on a symmetric Li||Li cell at a constant current density of  $50 \mu\text{A cm}^{-2}$  with a step time of 30 min between charge and discharge (see higher magnification in Fig. S9†). All electrochemical tests were carried out at 40 °C.

metric curves and from the fitting of the Nyquist plots recorded before and after polarization (insets in Fig. S7†) are reported in Table S3,† revealing a  $t^+$  approaching unity for cells with varying thicknesses of the B35 membranes, as expected for SIPEs. The stability of B35 towards aging in contact with lithium metal was evaluated by EIS measurements performed on symmetric Li||Li cells, as displayed in Fig. 3g (Nyquist plots) and Fig. 3h (evolution of the electrode|electrolyte interphase resistance, *i.e.*,  $R_i$ ; see Table S4† for the actual values). The data reveal a rather stable  $R_i$  between 210 and 230 Ω during the first 12 h after cell assembly, while a

gradual growth up to 300 Ω is observed after 7 days, indicating the consolidation of a low-resistive SEI. The stability of the interphase is further proven by EIS analyses performed on the same cells after galvanostatic Li stripping/plating tests at 10 and  $50 \mu\text{A cm}^{-2}$ , revealing an  $R_i$  of about 300 Ω (Fig. S8 and Table S5†). A magnification of the corresponding voltage profiles (Fig. S8a†) shows a very stable and flat voltage response, further corroborating the single-ion conducting behavior in agreement with the  $\text{Li}^+$  transference number of essentially unity. In addition, the long-term galvanostatic Li stripping/plating test depicted in Fig. 3i demonstrates the



ability of B35 to withstand extensive cycling in symmetric Li||Li cell over 1000 h at  $50 \mu\text{A cm}^{-2}$ , maintaining a rather stable overpotential of less than 130 mV during the whole experiment. A magnification of the Li stripping/plating voltage profiles is reported in Fig. S9,<sup>†</sup> showing a very minor slope of the generally square-shaped profiles, which likely originates from somewhat slower  $\text{Li}^+$  transport across the SEI layer on the lithium-metal electrodes.<sup>66</sup>

The B35 membrane is subsequently evaluated in completely fluorine-free Li||LFP cells. Fig. 4 displays the rate capability tests, which were performed with LFP electrodes having two different active material mass loadings of either  $2.8 \pm 0.2 \text{ mg cm}^{-2}$  or  $8.2 \pm 0.2 \text{ mg cm}^{-2}$ , with the latter incorporating 7 wt% dry SIPE. The cells were galvanostatically cycled at increasing C rates from 0.05C to 2C ( $1\text{C} = 170 \text{ mA g}^{-1}$ ). The cycling trend in Fig. 4a shows, for both the LFP cathodes, a remarkable discharge capacity in the  $145\text{--}155 \text{ mA h g}^{-1}$  range at 0.05C (*i.e.*, 85–91% of the theoretical capacity), with subsequent minor decay, as demonstrated by the capacity of  $134 \text{ mA h g}^{-1}$  delivered at 0.2C. In addition, the low-loading LFP cathode still

exhibits capacities of  $111 \text{ mA h g}^{-1}$  and  $74 \text{ mA h g}^{-1}$  at 0.5C and 1C, respectively, and both the electrodes recover a capacity of around  $130 \text{ mA h g}^{-1}$  when the current is reduced back to 0.2C after 30 cycles. The charge/discharge profiles related to the low-loading LFP cathode (Fig. 4b) display the first charge at 0.05C centered at  $\sim 3.46 \text{ V}$  (de-lithiation of LFP), followed by a sloping discharge curve at  $\sim 3.39 \text{ V}$  (lithiation of LFP),<sup>67</sup> while an increase of polarization can be observed in concomitance with the rising current as expected by the ohmic resistance increment, despite the cell still presents electrochemical activity at a relatively high current of 2C. Notably, the voltage profiles related to the high-loading LFP cathode (Fig. 4c) show only slightly higher polarization at 0.05C for charge/discharge processes, occurring at  $\sim 3.46$  and  $\sim 3.36 \text{ V}$ , respectively, while revealing almost total deactivation of the electrochemical process already at 0.5C, indicating a rate capability extended up to 0.2C.

Long-term galvanostatic cycling tests of Li|B35|LFP cells are depicted in Fig. 5. The low-mass-loading LFP cathodes (around  $2.8 \text{ mg cm}^{-2}$ ) were subjected to measurements either at 0.2C

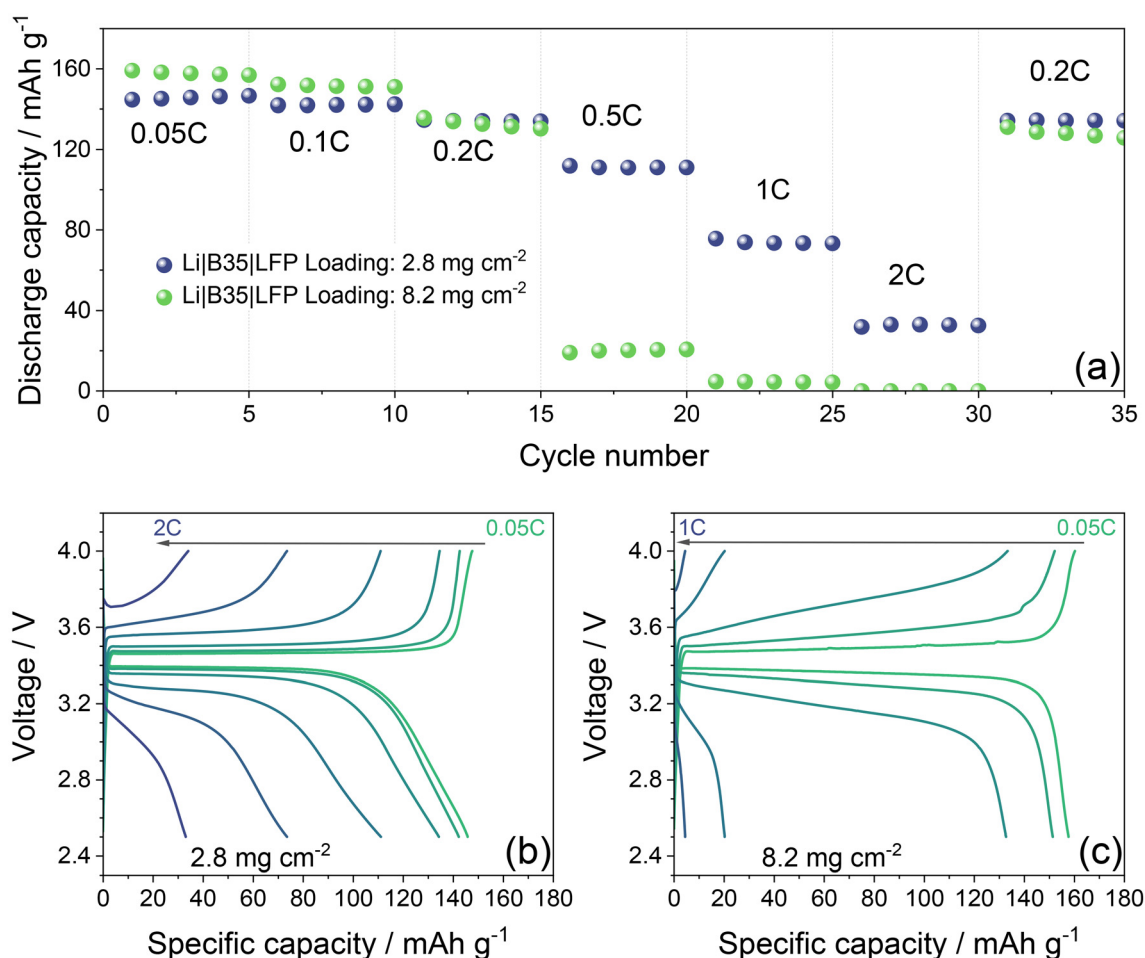


**Fig. 4** (a) Specific capacity as a function of cycle number and (b and c) voltage profiles for the rate capability tests performed via galvanostatic cycling on Li|B35|LFP cells at increasing C rates in the 2.5–4.0 V voltage range using an LFP areal loading of either (b) 2.8 or (c)  $8.2 \text{ mg cm}^{-2}$ . All tests were carried out at  $40^\circ\text{C}$ .

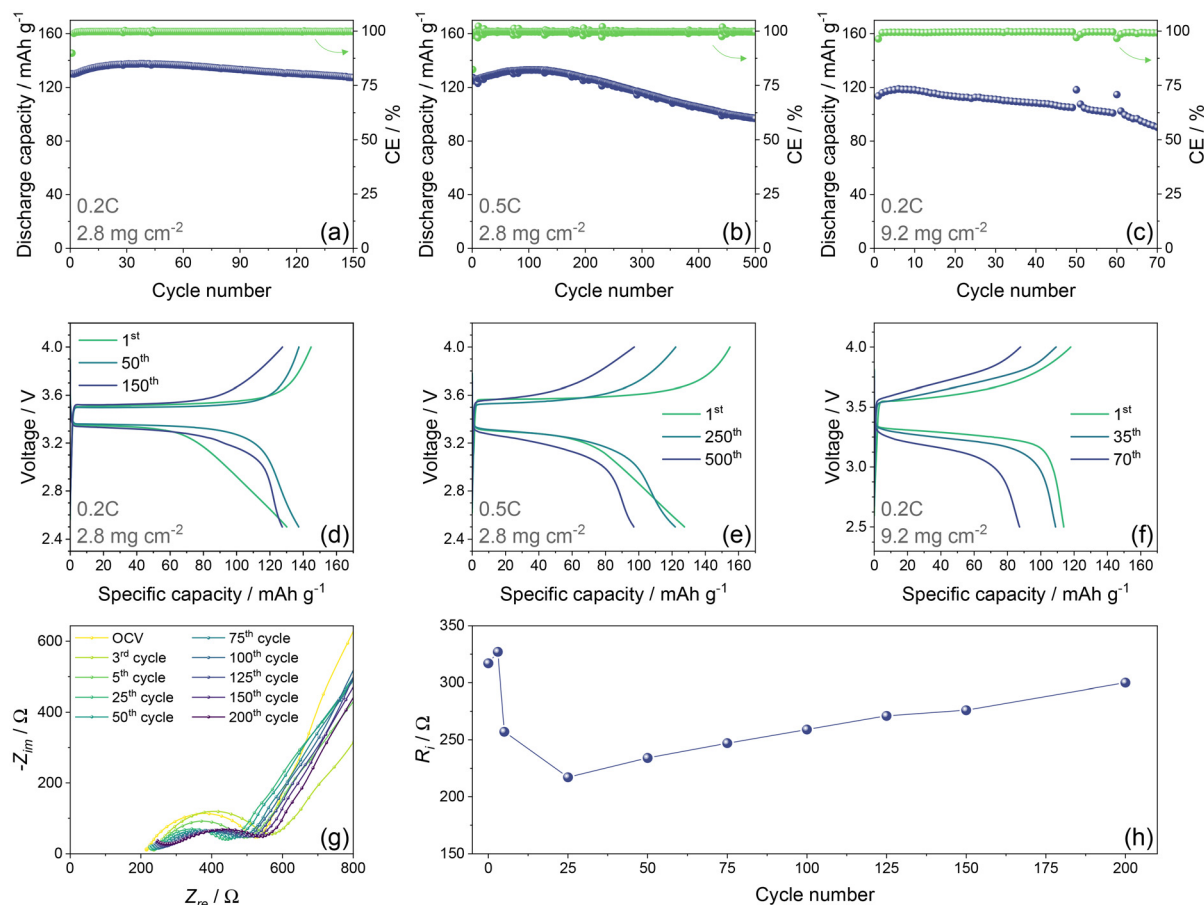


**Fig. 5** (a–c) Plots of the specific capacity as a function of cycle number (the CE is displayed on the right y-axes) and (d–f) voltage profiles for the long-term galvanostatic cycling tests performed on Li[B35]LFP cells with (a and d) an LFP mass loading of  $2.8 \text{ mg cm}^{-2}$  at 0.2C and (b and e) at 0.5C, and (c and f) with an LFP mass loading of  $9.2 \text{ mg cm}^{-2}$  at 0.2C. (g) Nyquist plots recorded by EIS upon cycling of a Li[B35]LFP cell at 0.5C with 3 activation cycles at 0.05C ( $2.8 \text{ mg cm}^{-2}$ ) and (h) the corresponding trend of  $R_i$  as a function of the cycle number obtained by NLLS fitting of the Nyquist plots (the actual data are reported in Table S6†). Voltage range for cycling tests: 2.5–4.0 V; EIS frequency range: 200 kHz–50 mHz. EIS voltage amplitude: 10 mV. All tests were carried out at 40 °C.

or 0.5C, while the LFP cathodes with a mass loading of about  $9.2 \text{ mg cm}^{-2}$  were cycled at 0.2C. The cycling trends reveal a maximum capacity of  $137 \text{ mA h g}^{-1}$  with 93% retention after 150 cycles for the low-loading electrode cycled at 0.2C (Fig. 5a), while the one cycled at 0.5C shows a cycle life up to 500 cycles with a maximum capacity of  $133 \text{ mA h g}^{-1}$  and 73% retention at the end of the test (Fig. 5b). The high-loading LFP cathode exhibits instead a delivered capacity of around  $120 \text{ mA h g}^{-1}$  with 75% retention after 70 cycles (Fig. 5c). In addition, all the cells demonstrate a coulombic efficiency (CE) exceeding 99% after the first cycle, subsequently maintained for the entire measurement. The lower initial CE observed for all the tests can be ascribed to the consolidation of the passivation layers, which would also explain the gradual increase of capacity during the first cycles. The corresponding voltage profiles (Fig. 5d–f) show for all the tests the development of single-plateau charge/discharge processes, including the expected increase in polarization when a higher C rate (*i.e.*, 0.5C in Fig. 5e) or a high mass loading cathode (Fig. 5f) is used. To

investigate the capacity decay upon long-term cycling in more detail, EIS was performed. Fig. 5g shows the Nyquist plots recorded for Li[B35]LFP cells upon cycling at 0.5C with LFP electrodes having an active material loading of  $2.8 \text{ mg cm}^{-2}$ . The corresponding trend for  $R_i$  as a function of the cycle number, obtained by NLLS fitting (see Table S6† for the actual data), is reported in Fig. 5h. The analysis reveals an increase in the interphase resistance during the first three activation cycles from 317 to 327 Ω and a subsequent drop to 257 Ω in the 5<sup>th</sup> cycle and to 217 Ω in the 25<sup>th</sup> cycle, which is in line with the initial growth of a resistive passivation layer, which then stabilizes and becomes less resistive upon cycling. Subsequently,  $R_i$  shows a steady, though minor, increase up to 300 Ω after 200 cycles. This behavior matches with the trend of the delivered capacity exhibited by these cells, as displayed in Fig. 5b, which shows a slight decrease after the first cycle, gradual growth and stabilization during the subsequent ~75 cycles, and a steady decrease until the end of the test. These reactions are apparently more pronounced when cycling the



cells at elevated temperatures and in the absence of F, which commonly results in the formation of very well passivating LiF,<sup>10</sup> while operating the cells at lower temperatures of, *e.g.*, 20 °C results in a significantly lower specific capacity owing to substantially higher polarization and interfacial resistance (Fig. S10†). Nonetheless, a comparison with other, comparable studies reported earlier<sup>25,48,68–72</sup> (Table S7†) reveals that the results achieved in this work are well comparable with the state of the art, especially when taking into account the considerably higher active material mass loading of the LFP electrodes studied herein, the absence of F,<sup>25,68–72</sup> and the lower cycling temperature with respect to other F-free configurations.<sup>48</sup>

To underline the great impact of transitioning to F-free SIPEs with regard to enhanced sustainability, we conducted a hazard and toxicity assessment (Appendix 1†) and compared this with an earlier reported F-containing SIPE using the same polysiloxane backbone (PSiOM; Appendix 2†).<sup>50</sup> For this purpose, we used the hazard traffic light (HTL) method to identify potential hotspots in the synthesis process. The SIPE membrane synthesis process shows multiple potential health hazards, including acute toxicity impacts (H300, H311, and H331), skin corrosion/irritation (H314), serious eye damage/irritation (H318), carcinogenicity (H350), and reproductive toxicity (H360), particularly associated with the precursors *N,N*-dimethylformamide, thionyl chloride, *tert*-butylcatechol, acetonitrile, triethylamine, and lithium hydroxide monohydrate for the synthesis of (4-styrene)sulfonylchloride and the synthesis of the LiSDM ionic side chain. Physical hazards (flammable liquid (H225)) are also associated with a few solvents (acetonitrile, triethylamine, and tetrahydrofuran) used for the synthesis of the LiSDM ionic side chain and the synthesis of the SIPE as such. However, the synthesis of the F-containing analogue PSiOM<sup>50</sup> provides similar potential health and physical hazards derived from the use of flammable liquids (H225), acute toxicity (H301, H311, and H331), skin corrosion (H314), serious eye damage/irritation (H318), carcinogenicity (H350), reproductive toxicity (H360), aspiration hazard (H304), and specific organ toxicity due to repetitive exposure (H372). Thus, critical hotspots in the synthesis of the F-free SIPE still remain, in particular for the synthesis of the LiSDM ionic side chain. Nevertheless, the F-containing PSiOM counterpart exhibits additional HTL impacts, a higher number of hazardous chemicals involved in the synthesis sub-processes (about 30% more), and the concerns linked to the environmental challenges derived from the F-containing species such as trifluoromethanesulfonamide, PVdF-*co*-hexafluoropropylene (PVdF-HFP), and fluoroethylene carbonate—the latter two being used for the preparation of the polymer electrolyte membranes.<sup>50</sup> In this context, Fig. 6 summarises the number of hazards based on the HTL results (see Appendix 1 and Appendix 2 for the details†) linked to the synthesis of both polymer electrolytes in terms of physical (Fig. 6a), health (Fig. 6b), and total overall hazards (Fig. 6c), showing the generally lower number of hazards for the F-free SIPE compared to the F-containing PSiOM. It is worth noting that data gaps in this case include the absence of hazard statements for poly

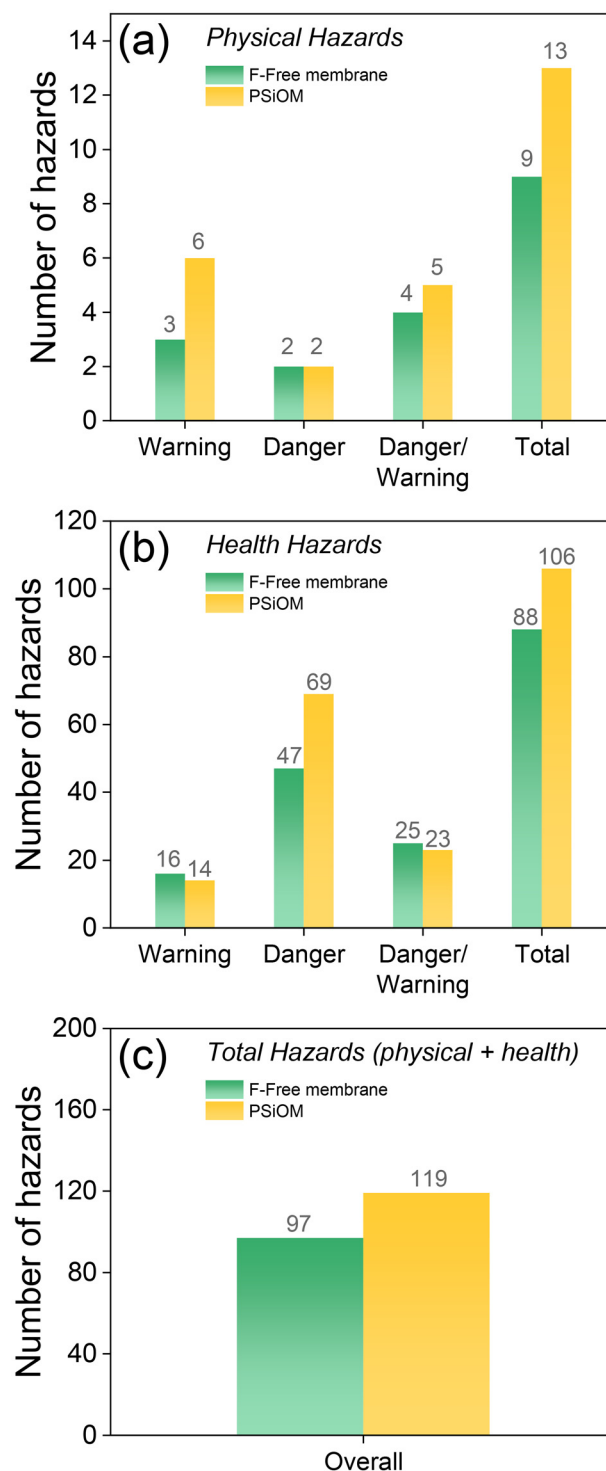


**Fig. 6** Overview of the number of hazards obtained by the HTL method linked to the F-free SIPE and the F-containing PSiOM (serving as the reference) in terms of (a) physical, (b) health, and (c) total hazards (expressed as the sum of physical and health hazards). The detailed HTL results are reported in Appendix 1† and Appendix 2† for the F-free SIPE and PSiOM, respectively.



(mercaptopropyl)methylsiloxane, PAN, and PVdF-HFP, which were not included in the HTL assessment. These gaps prevent a proper comparison between the electrolytes in terms of environmental hazards, which were thereby excluded from Fig. 6, and make the calculation of quantitative total hazard points (THPs) presently not meaningful. Nevertheless, the given toxicity assessment highlights the remaining challenges for the synthesis of truly sustainable SIPEs and sets a benchmark for future studies, while also evidencing the progress achieved compared to the F-containing counterpart.

## Conclusions

Herein, a novel fluorine-free SIPE is synthesized and characterized. The electrolyte membrane benefited from a PAN content of 35 wt% and incorporated 50 wt% PC solvent as a molecular transporter. The self-standing membrane presented a transference number of around 1, an ionic conductivity of over  $10^{-4}$  S  $\text{cm}^{-1}$  and stability up to 4.2 V vs.  $\text{Li}^+/\text{Li}$  at 40 °C. EIS performed upon aging on  $\text{Li}||\text{Li}$  cells revealed the growth of an electrode|electrolyte interphase with low resistance, while Li stripping/plating tests showed remarkable cyclability over 1000 h with the corresponding overvoltage as low as 130 mV. Galvanostatic cycling tests on  $\text{Li}||\text{LFP}$  cells revealed a good rate capability up to 1C and a cycle life of 500 cycles for electrodes with an active material loading of 2.8  $\text{mg cm}^{-2}$ , and capacities approaching 120  $\text{mA h g}^{-1}$  when a loading as high as 9.2  $\text{mg cm}^{-2}$  was used. The performance achieved herein is comparable to that of previously reported fluorinated SIPEs and may thus pave the way towards the development of well-performing, safe and environmentally friendly polymer electrolytes for LMBs.

## Data availability

The data supporting this article have been included as part of the ESI.†

## Conflicts of interest

There are no conflicts to declare.

## Acknowledgements

The authors would like to acknowledge financial support from the Federal Ministry of Education and Research (BMBF) within the FB2-Poly project (03XP0429B) and the Helmholtz Association.

## References

- 1 A. Z. Al Shaqsi, K. Sopian and A. Al-Hinai, *Energy Rep.*, 2020, **6**, 288–306.
- 2 D. Larcher and J.-M. Tarascon, *Nat. Chem.*, 2015, **7**, 19–29.
- 3 J. B. Goodenough and Y. Kim, *Chem. Mater.*, 2010, **22**, 587–603.
- 4 T. Kim, W. Song, D.-Y. Son, L. K. Ono and Y. Qi, *J. Mater. Chem. A*, 2019, **7**, 2942–2964.
- 5 J. Xu, X. Cai, S. Cai, Y. Shao, C. Hu, S. Lu and S. Ding, *Energy Environ. Mater.*, 2023, **6**, e12450.
- 6 S. Xia, X. Wu, Z. Zhang, Y. Cui and W. Liu, *Chem*, 2019, **5**, 753–785.
- 7 H. Wang, L. Sheng, G. Yasin, L. Wang, H. Xu and X. He, *Energy Storage Mater.*, 2020, **33**, 188–215.
- 8 A. Varzi, K. Thanner, R. Scipioni, D. Di Lecce, J. Hassoun, S. Dörfler, H. Altheus, S. Kaskel, C. Prehal and S. A. Freunberger, *J. Power Sources*, 2020, **480**, 228803.
- 9 H. Wu, H. Jia, C. Wang, J. Zhang and W. Xu, *Adv. Energy Mater.*, 2021, **11**, 2003092.
- 10 X. He, D. Bresser, S. Passerini, F. Baakes, U. Krewer, J. Lopez, C. T. Mallia, Y. Shao-Horn, I. Cekic-Laskovic, S. Wiemers-Meyer, F. A. Soto, V. Ponce, J. M. Seminario, P. B. Balbuena, H. Jia, W. Xu, Y. Xu, C. Wang, B. Horstmann, R. Amine, C.-C. Su, J. Shi, K. Amine, M. Winter, A. Latz and R. Kostecki, *Nat. Rev. Mater.*, 2021, **6**, 1036–1052.
- 11 L. He, Q. Sun, L. Lu and S. Adams, *ACS Appl. Mater. Interfaces*, 2021, **13**, 34320–34331.
- 12 X. Zhang, A. Wang, X. Liu and J. Luo, *Acc. Chem. Res.*, 2019, **52**, 3223–3232.
- 13 M. K. Aslam, Y. Niu, T. Hussain, H. Tabassum, W. Tang, M. Xu and R. Ahuja, *Nano Energy*, 2021, **86**, 106142.
- 14 D. Wang, W. Zhang, W. Zheng, X. Cui, T. Rojo and Q. Zhang, *Adv. Sci.*, 2017, **4**, 1600168.
- 15 Y. Cheng, J. Chen, Y. Chen, X. Ke, J. Li, Y. Yang and Z. Shi, *Energy Storage Mater.*, 2021, **38**, 276–298.
- 16 H. Liu, J. Di, P. Wang, R. Gao, H. Tian, P. Ren, Q. Yuan, W. Huang, R. Liu, Q. Liu and M. Feng, *Carbon Energy*, 2022, **4**, 654–664.
- 17 H. Zhang, G. G. Eshetu, X. Judez, C. Li, L. M. Rodriguez-Martinez and M. Armand, *Angew. Chem., Int. Ed.*, 2018, **57**, 15002–15027.
- 18 R. S. Thompson, D. J. Schroeder, C. M. López, S. Neuhold and J. T. Vaughey, *Electrochem. Commun.*, 2011, **13**, 1369–1372.
- 19 Z. Ge, N. Chen, R. Wang, R. Ma, B. Fan, D. Le Coq, X. Zhang, H. Ma and B. Xue, *Chem. Eng. J.*, 2023, **467**, 143409.
- 20 N. T. Temesgen, H. K. Bezabh, M. A. Weret, K. N. Shitaw, Y. Nikodimos, B. W. Taklu, K. Lakshmanan, S.-C. Yang, S.-K. Jiang, C.-J. Huang, S.-H. Wu, W.-N. Su and B. J. Hwang, *J. Power Sources*, 2023, **556**, 232462.
- 21 Y. Wu, J. Xu, P. Lu, J. Lu, L. Gan, S. Wang, R. Xiao, H. Li, L. Chen and F. Wu, *Adv. Energy Mater.*, 2023, **13**, 2301336.
- 22 X. Zhang, J. Wang, D. Hu, W. Du, C. Hou, H. Jiang, Y. Wei, X. Liu, F. Jiang, J. Sun, H. Yuan and X. Huang, *Energy Storage Mater.*, 2024, **65**, 103089.
- 23 A. Mauger, C. M. Julien, A. Paoletta, M. Armand and K. Zaghib, *Materials*, 2019, **12**, 3892.
- 24 A. Mayer, D. Steinle, S. Passerini and D. Bresser, *Nanotechnology*, 2022, **33**, 062002.



- 25 X. Dong, Z. Chen, X. Gao, A. Mayer, H.-P. Liang, S. Passerini and D. Bresser, *J. Energy Chem.*, 2023, **80**, 174–181.
- 26 Z. Song, F. Chen, M. Martinez-Ibañez, W. Feng, M. Forsyth, Z. Zhou, M. Armand and H. Zhang, *Nat. Commun.*, 2023, **14**, 4884.
- 27 J. Chattopadhyay, T. S. Pathak and D. M. F. Santos, *Polymers*, 2023, **15**, 3907.
- 28 X. Zhao, C. Wang, H. Liu, Y. Liang and L. Fan, *Batteries Supercaps*, 2023, **6**, e202200502.
- 29 P. Lennartz, B. A. Paren, A. Herzog-Arbeitman, X. C. Chen, J. A. Johnson, M. Winter, Y. Shao-Horn and G. Brunklaus, *Joule*, 2023, **7**, 1471–1495.
- 30 V. Marangon, L. Minnetti, E. Barcaro and J. Hassoun, *Chem. – Eur. J.*, 2023, **29**, e202301345.
- 31 K. Timachova, H. Watanabe and N. P. Balsara, *Macromolecules*, 2015, **48**, 7882–7888.
- 32 M. Doyle, T. F. Fuller and J. Newman, *Electrochim. Acta*, 1994, **39**, 2073–2081.
- 33 X.-G. Sun and J. B. Kerr, *Macromolecules*, 2006, **39**, 362–372.
- 34 K. M. Diederichsen, E. J. McShane and B. D. McCloskey, *ACS Energy Lett.*, 2017, **2**, 2563–2575.
- 35 C. Shan, Y. Wang, M. Liang, K. Lu, C. Xiong, W. Hu and B. Liu, *Energy Storage Mater.*, 2023, **63**, 102955.
- 36 H. Yuan, J. Luan, Z. Yang, J. Zhang, Y. Wu, Z. Lu and H. Liu, *ACS Appl. Mater. Interfaces*, 2020, **12**, 7249–7256.
- 37 S. Kondou, M. Abdullah, I. Popov, M. L. Martins, L. A. O'Dell, H. Ueda, F. Makhlooghiyazad, A. Nakanishi, T. Sudoh, K. Ueno, M. Watanabe, P. Howlett, H. Zhang, M. Armand, A. P. Sokolov, M. Forsyth and F. Chen, *J. Am. Chem. Soc.*, 2024, **146**, 33169–33178.
- 38 D. Fraile-Insagurbe, N. Boaretto, I. Aldalur, I. Raposo, F. J. Bonilla, M. Armand and M. Martínez-Ibañez, *Nano Res.*, 2023, **16**, 8457–8468.
- 39 Z. Chen, D. Steinle, H.-D. Nguyen, J.-K. Kim, A. Mayer, J. Shi, E. Paillard, C. Iojoiu, S. Passerini and D. Bresser, *Nano Energy*, 2020, **77**, 105129.
- 40 G. Hernández, R. Mogensen, R. Younesi and J. Mindemark, *Batteries Supercaps*, 2022, **5**, e202100373.
- 41 A. Mayer, H.-D. Nguyen, A. Mariani, T. Diemant, S. Lyonard, C. Iojoiu, S. Passerini and D. Bresser, *ACS Macro Lett.*, 2022, **11**, 982–990.
- 42 J. Glüge, M. Scheringer, I. T. Cousins, J. C. DeWitt, G. Goldenman, D. Herzke, R. Lohmann, C. A. Ng, X. Trier and Z. Wang, *Environ. Sci.: Processes Impacts*, 2020, **22**, 2345–2373.
- 43 G. Hernández, A. J. Naylor, Y.-C. Chien, D. Brandell, J. Mindemark and K. Edström, *ACS Sustainable Chem. Eng.*, 2020, **8**, 10041–10052.
- 44 Z. Jiang, C. Li, T. Yang, Y. Deng, J. Zou, Q. Zhang and Y. Li, *ACS Energy Lett.*, 2024, **9**, 1389–1396.
- 45 H. Markusson, P. Johansson and P. Jacobsson, *Electrochem. Solid-State Lett.*, 2005, **8**, A215.
- 46 A. Fu, J. Lin, Z. Zhang, C. Xu, Y. Zou, C. Liu, P. Yan, D.-Y. Wu, Y. Yang and J. Zheng, *ACS Energy Lett.*, 2022, **7**, 1364–1373.
- 47 M. Martinez-Ibañez, E. Sanchez-Diez, L. Qiao, L. Meabe, A. Santiago, H. Zhu, L. A. O'Dell, J. Carrasco, M. Forsyth, M. Armand and H. Zhang, *Batteries Supercaps*, 2020, **3**, 738–746.
- 48 C. Han, L. Qiao, G. Xu, G. Chen, K. Chen, S. Zhang, J. Ma, S. Dong, X. Zhou, Y. Han, Z. Cui and G. Cui, *ACS Appl. Mater. Interfaces*, 2024, **16**, 48792–48802.
- 49 B. R. Johnson, A. Sankara Raman, A. Narla, S. Jhulki, L. Chen, S. R. Marder, R. Ramprasad, K. Turcheniuk and G. Yushin, *ACS Omega*, 2024, **9**, 15410–15420.
- 50 H. Liang, M. Zarrabeitia, Z. Chen, S. Jovanovic, S. Merz, J. Granwehr, S. Passerini and D. Bresser, *Adv. Energy Mater.*, 2022, **12**, 2200013.
- 51 X. Zhong, J. Han, L. Chen, W. Liu, F. Jiao, H. Zhu and W. Qin, *Appl. Surf. Sci.*, 2021, **553**, 149564.
- 52 X. Huang, J.-Y. Guo, J. Yang, Y. Xia, Y.-F. Zhang, P. Fu and F.-P. Du, *Polymer*, 2022, **254**, 125066.
- 53 S. Zhao, Y. Zhang, H. Pham, J.-M. Y. Carrillo, B. G. Sumpter, J. Nanda, N. J. Dudney, T. Saito, A. P. Sokolov and P.-F. Cao, *ACS Appl. Energy Mater.*, 2020, **3**, 12540–12548.
- 54 S. Xie, A. Nikolaev, O. A. Nordness, L. C. Llanes, S. D. Jones, P. M. Richardson, H. Wang, R. J. Clément, J. Read De Alaniz and R. A. Segalman, *Macromolecules*, 2022, **55**, 5723–5732.
- 55 Y. A. Min'ko, N. V. Belina, V. V. Sushev, G. K. Fukin, M. P. Bubnov and A. N. Kornev, *J. Organomet. Chem.*, 2007, **692**, 4157–4160.
- 56 S. Ramesh, C.-W. Liew, E. Morris and R. Durairaj, *Thermochim. Acta*, 2010, **511**, 140–146.
- 57 A. C.-Y. Wong and F. Lam, *Polym. Test.*, 2002, **21**, 691–696.
- 58 A. Mayer, T. Ates, A. Varzi, S. Passerini and D. Bresser, *Front. Chem.*, 2022, **10**, 974202.
- 59 H.-D. Nguyen, G.-T. Kim, J. Shi, E. Paillard, P. Judeinstein, S. Lyonard, D. Bresser and C. Iojoiu, *Energy Environ. Sci.*, 2018, **11**, 3298–3309.
- 60 A. Mayer, A. Mariani, X. Dong, G. Vansse, P. Theato, C. Iojoiu, S. Passerini and D. Bresser, *Macromolecules*, 2023, **56**, 2505–2514.
- 61 M. A. Schiavon, N. A. Armelin and I. V. P. Yoshida, *Mater. Chem. Phys.*, 2008, **112**, 1047–1054.
- 62 H. Zhang, L. Quan, A. Gao, Y. Tong, F. Shi and L. Xu, *Polymers*, 2020, **12**, 221.
- 63 M.-J. Yu, Y.-J. Bai, C.-G. Wang, Y. Xu and P.-Z. Guo, *Mater. Lett.*, 2007, **61**, 2292–2294.
- 64 S. Zugmann, M. Fleischmann, M. Amereller, R. M. Gschwind, H. D. Wiemhöfer and H. J. Gores, *Electrochim. Acta*, 2011, **56**, 3926–3933.
- 65 J. Evans, C. A. Vincent and P. G. Bruce, *Polymer*, 1987, **28**, 2324–2328.
- 66 K. Borzutzki, J. R. Nair, M. Winter and G. Brunklaus, *ACS Appl. Mater. Interfaces*, 2022, **14**, 5211–5222.
- 67 V. Marangon, L. Minnetti, M. Adami, A. Barlini and J. Hassoun, *Energy Fuels*, 2021, **35**, 10284–10292.
- 68 Q. Pan, S. Jiang, Z. Li, Y. Liu, Y. Du, N. Zhao, Y. Zhang and J.-M. Liu, *J. Membr. Sci.*, 2021, **636**, 119601.



- 69 Y. Chen, H. Ke, D. Zeng, Y. Zhang, Y. Sun and H. Cheng, *J. Membr. Sci.*, 2017, **525**, 349–358.
- 70 Y. Chen, C. Li, D. Ye, Y. Zhang, H. Bao and H. Cheng, *J. Membr. Sci.*, 2021, **620**, 118926.
- 71 K. Deng, S. Wang, S. Ren, D. Han, M. Xiao and Y. Meng, *J. Power Sources*, 2017, **360**, 98–105.
- 72 C. Li, B. Qin, Y. Zhang, A. Varzi, S. Passerini, J. Wang, J. Dong, D. Zeng, Z. Liu and H. Cheng, *Adv. Energy Mater.*, 2019, **9**, 1803422.

